

Wafer-to-Wafer Bonding: Part: I - The Coupled Physics Problem and the 2D Finite Element Implementation

Kamalendu Ghosh^{a,1,*}, Bhavesh Shrimali^{b,1,*}, Subin Jeong^c

^a *Visiting Researcher, Aerospace Engineering, University of Illinois at Urbana-Champaign, Illinois 61801, USA*

^b *University of Illinois at Urbana-Champaign, Illinois 61801, USA*

^c *Department of Mechanical Engineering, Texas A & M University, College Station, TX 77840*

Abstract

Wafer-to-wafer (WxW) bonding is a key enabler for three-dimensional integration, including hybrid bonding for fine-pitch Cu–Cu interconnects. During bonding, wafer deformation and the air entrapped between the wafers interact through a strongly coupled, time-dependent fluid–structure interaction (FSI) that can produce non-intuitive bonding dynamics and process sensitivities. This paper develops a mathematically consistent reduced-order model for WxW bonding by deriving a Kirchhoff–Love plate equation for wafer bending from three-dimensional linear elasticity and coupling it to a Reynolds lubrication equation for the inter-wafer air film. The resulting nonlinear plate–Reynolds system is discretized and solved monolithically in the high-performance FEniCSx framework using a C^0 interior-penalty formulation for the fourth-order plate operator, standard continuous Galerkin discretization for the pressure field, implicit time integration, and a Newton solver with automatic differentiation. Simulations reproduce experimentally reported probe-displacement histories for multiple initial gaps and verify force equilibrium at the bond front, where the Reynolds pressure acts as an effective contact reaction. Parametric studies reveal nonlinear, and in some cases non-monotonic, sensitivities of bonding-front kinetics to the initial gap, air viscosity, and interfacial energy, providing actionable trends for process optimization.

Keywords: Wafer-to-Wafer Bonding, Hybrid Bonding, Fusion Bonding, 3D Integration, Advanced Packaging, Finite Element, FEniCSx

1. Introduction

Wafer-to-Wafer (WxW) bonding has emerged as a cornerstone technology for next-generation semiconductor packaging, enabling three-dimensional integrated circuit (3D-IC) stacking, High Bandwidth Memory (HBM), MEMS fabrication, and photonic device integration [1, 2]. Unlike traditional bump-based stacking, which introduces inter-die gaps of approximately $30\ \mu\text{m}$ and is limited to interconnect pitches above $10\ \mu\text{m}$, (hybrid) WxW bonding achieves direct Cu-to-Cu connections with pitches below $10\ \mu\text{m}$, enabling substantially higher I/O density, reduced package dimensions, lower electrical resistance and superior thermal conductivity [1]. These attributes translate directly into higher bandwidth, improved signal integrity, reduced power consumption, and enhanced heat dissipation—all critical requirements for enabling miniaturization of packages and modern HBM architectures. Despite this transformative potential, WxW bonding involved high process sensitivities: even sub-micron particulate contamination can nucleate voids at the bond interface, leading to

*These authors contributed equally to this work.

Email addresses: kamalendugho@micron.com, kamalendu.iitkgp@gmail.com (Kamalendu Ghosh), bhavesh.shrimali@gmail.com (Bhavesh Shrimali), sooibing@tamu.edu (Subin Jeong)

¹Work was done prior to the authors started working at Micron

delamination, incomplete bonding, high overlays, and degraded mechanical and electrical integrity. Furthermore, the governing physics of the bonding process involve a strongly coupled, nonlinear fluid–structure interaction that can give rise to non-intuitive behaviors, such as non-monotonic relationships between overlay and initial bond gap. Developing a rigorous predictive model of the bonding process is therefore not merely of academic interest but of direct industrial relevance, as it provides a pathway to understanding and mitigating these failure mechanisms.

The dynamics of the bonding front have been studied since the seminal work of Rieutord et al. [3], who proposed a model relating the bonding front velocity to the surface adhesion energy and the viscous drag of air escaping the shrinking gap between the wafers. This competition between elastic driving forces and viscous resistance was later formalized as a coupled Fluid–Structure Interaction (FSI) problem by Navarro et al. [4], wherein the elastic deformation of the wafer governs the gap geometry and the resulting pressure field in turn loads the wafer. The dynamics of the bonding wave has also been analytically examined by Radisson et al. [5], who modeled the propagation speed of the bonding front as a function of the material and geometric parameters. More recent efforts have employed general-purpose finite element methods to model various aspects of the bonding process, including bonding wave propagation and cavity-induced deformation modes [6–8], thermo-mechanical effects in glass-frit bonding [9], and Cu pad expansion in hybrid bonding [10]. Together, these studies have demonstrated the viability of the FSI framework for capturing the essential physics of WxW bonding.

Despite this body of work, existing models share three common limitations: (a) the FSI problem and mechanical sub-problems are treated with insufficient mathematical rigor; (b) the nonlinear and time-dependent nature of the governing equations is neither sufficiently acknowledged nor systematically analyzed; and (c) the computational implementation of the coupled multiphysics problem is not described in sufficient detail to enable reproducibility. Prior formulations typically employ simplified plate models without systematically deriving them from the three-dimensional governing equations of linear elasticity and without clearly stating the assumptions under which such reductions are valid [4, 6]. The three-dimensional balance of linear momentum, the Kirchhoff–Love kinematic hypothesis, and the derivation of the flexural rigidity are rarely made explicit or connected to a well-posed boundary value problem. Furthermore, the *nonlinear nature* of the coupled system has been largely overlooked: the two-way coupling between wafer deflection and air pressure (between the two wafers) yields a genuinely nonlinear, time-dependent FSI problem whose solution behavior is far from intuitive. Non-intuitive phenomena—such as pressure-induced retardation of the bond front and the non-monotone dependence of bonding wave speed on initial bond gap—have not been rigorously analyzed or attributed to the structure of the governing equations.

The present work addresses these shortcomings by developing a mathematically rigorous, fully coupled FSI formulation for WxW bonding, implemented in the high-performance FEniCSx finite element framework [11, 12]. Starting from the three-dimensional equations of linear elasticity for an isotropic wafer, we perform a systematic reduction to the classical Kirchhoff–Love plate equation via through-thickness integration [13], making all assumptions and their validity criteria explicit. The trapped air is governed by the Reynolds lubrication equation, and the two-way coupling—wherein the wafer deflection and its rate determine the air pressure, which as a distributed transverse load on the wafer—is preserved in full. The resulting *inherently nonlinear* coupled equations, and the results presented in Section 4 demonstrate several counter-intuitive implications of this nonlinearity that have not been previously reported in the WxW bonding literature. The implementation leverages the FEniCSx framework [11, 14–16], which has proven effective for analogous nonlinear multiphysics problems including nonlinear viscoelasticity [17, 18] and dielectric elastomers [19].

The remainder of this paper is organized as follows. Section 2 presents the complete mathematical formulation, beginning with the three-dimensional governing equations and proceeding through their systematic reduction to the two-dimensional coupled plate–Reynolds system. Section 3 de-

scribes finite element discretization and FEniCSx implementation. Section 4 presents numerical results, including validation studies and the non-intuitive physical phenomena arising from the nonlinear coupling. Section 5 concludes with a summary and directions for future work.

2. Theory

The mechanics governing Wafer-to-Wafer (WxW) bonding are characterized by a coupled Fluid-Structure Interaction (FSI) problem. Consider, two wafers in their undeformed initial configurations at time, $t = 0$, within a Cartesian coordinate system, positioned coaxially by the bonding apparatus on the top and bottom chuck occupying domains Ω_{top} and Ω_{bot} respectively, such that $\Omega_{top} = \{\mathbf{X} \in \mathbb{R}^3 : X_1^2 + X_2^2 \leq R^2, -t_w \leq X_3 \leq 0\}$ and $\Omega_{bot} = \{\mathbf{X} \in \mathbb{R}^3 : X_1^2 + X_2^2 \leq R^2, -t_w - h_0 \leq X_3 \leq -h_0\}$. The top wafer's center is located at $(0,0,-t_w/2)$, and the center of the top surface of the bottom wafer is at $(0,0,-t_w/2 - h_0)$, resulting in an initial separation distance h_0 between the bottom surface of the top wafer and the top surface of the bottom wafer. A thin layer of air is entrapped within the interstitial gap between the wafers. At this stage, it is useful to define the following regions, as illustrated in Fig. 1

$$\left\{ \begin{array}{ll} \partial\Omega_{top}^u = \{\mathbf{X} : X_1^2 + X_2^2 \leq R^2, X_3 = 0\}, & \text{Top surface of the Upper wafer} \\ \partial\Omega_{top}^l = \{\mathbf{X} : X_1^2 + X_2^2 \leq R^2, X_3 = -t_w\}, & \text{Bottom surface of the Upper wafer} \\ \partial\Omega_{top}^{lat} = \{\mathbf{X} : X_1^2 + X_2^2 = R^2, 0 \leq X_3 \leq -t_w\}, & \text{Lateral curved surface of the Upper wafer} \\ \partial\Omega_{bot}^u = \{\mathbf{X} : X_1^2 + X_2^2 \leq R^2, X_3 = -t_w/2 - h_0\}, & \text{Top surface of bottom wafer} \\ \partial\Omega_{bot}^l = \{\mathbf{X} : X_1^2 + X_2^2 \leq R^2, X_3 = -t_w - h_0\}, & \text{Bottom surface of the wafer on the bottom.} \end{array} \right. \quad (1)$$

Here and throughout, $\Omega_{top} \subset \mathbb{R}^3$ denotes the three-dimensional reference domain occupied by the top wafer, while

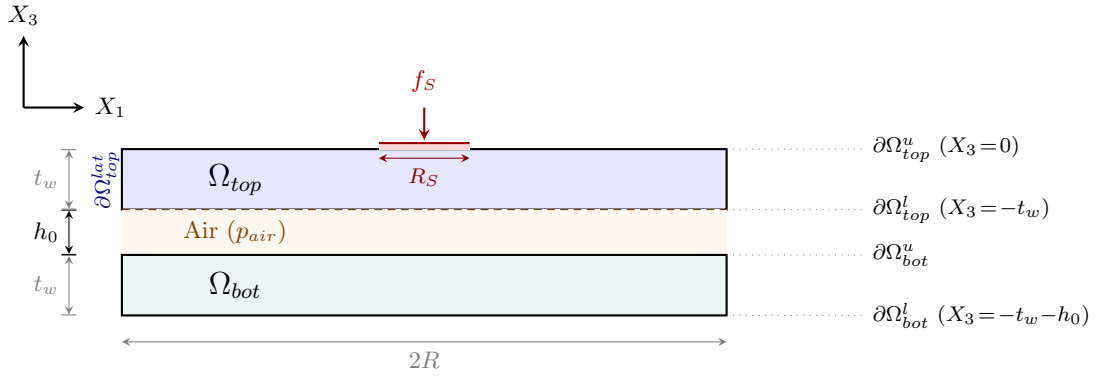
$$\omega = \{\bar{\mathbf{x}} = (X_1, X_2) \in \mathbb{R}^2 : X_1^2 + X_2^2 \leq R^2\} \quad (2)$$

denotes the two-dimensional mid-surface of the top wafer, obtained by projecting Ω_{top} onto the plane $X_3 = 0$.²

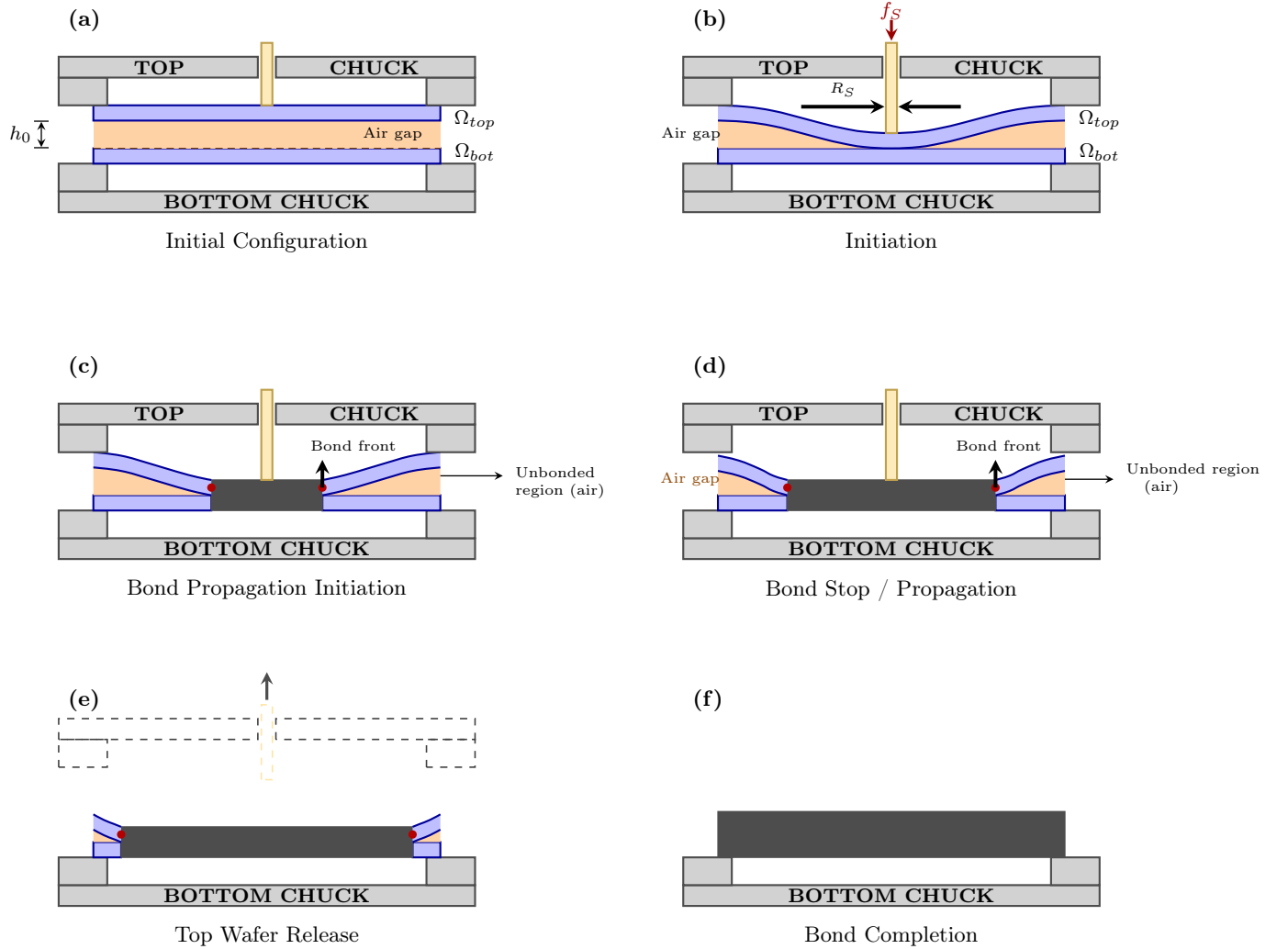
The subsequent bonding process encompasses the following four stages:

- **Initiation:** The process commences when a striker of radius R_S applies a localized force, $\mathbf{f}_S(\mathbf{X}, t) = f_S(\mathbf{X}, t)\mathbf{e}_3$ at time $t = 0$, where $\mathbf{X} \in \partial\Omega_S = \{\mathbf{X} \in \partial\Omega_{top}^u : X_1^2 + X_2^2 \leq R_S^2, X_3 = 0\}$, to the central region of the top wafer. This applied force induces a deformation in the top wafer, causing it to make initial physical contact with the bottom wafer at the point of maximum deflection and thereby modifying the effective separation $h(\mathbf{X}, t)$ between the wafers from its initial value $h(\mathbf{X}, t) = h_0$.
- **Bond Propagation:** Following initiation, the bond front propagates radially outward. The interfacing surfaces of both wafers undergo a pretreatment process (e.g., plasma activation) to establish attractive interfacial forces $f_B(\mathbf{X}, h(\mathbf{X}, t))$. These forces become significant when the local separation between the wafer surfaces reduces below a critical threshold δ such that

²The three-dimensional governing equations are posed on Ω_{top} , while the reduced plate model operates on ω as will be described in Section 2.2.



(a) Cross-sectional view (X_1 - X_3 plane) of the initial undeformed configuration. The top wafer Ω_{top} and bottom wafer Ω_{bot} are separated by an air gap of height h_0 . Boundary surfaces $\partial\Omega_{top}^{u,l}$ and $\partial\Omega_{bot}^{u,l}$ are labeled.



(b) Schematic of the wafer-to-wafer bonding process (cross-sectional view): (a) initial configuration with air gap h_0 between wafers Ω_{top} and Ω_{bot} ; (b) a striker applies force f_S to initiate contact at the center; (c) bond front begins to propagate radially outward from the contact zone; (d) bond front continues to advance while entrapped air is expelled; (e) the top wafer is released from the chuck and the striker is retracted; (f) full bonding across the entire interface.

Figure 1: (a) Cross-sectional view of the initial domain configuration showing the top wafer Ω_{top} and the bottom wafer Ω_{bot} separated by an air gap of height h_0 , and (b) schematic of the six stages of the wafer-to-wafer bonding process.

$$f_B(\mathbf{X}, h(\mathbf{X}, t)) = f_B(\mathbf{X}, h) = \begin{cases} = f_{BE}, & \text{if } h(\mathbf{X}, t) \leq \delta \\ = 0, & \text{otherwise.} \end{cases} \quad (3)$$

Consequently, these attractive forces draw the top wafer progressively towards the bottom wafer, concurrently expelling the entrapped air from the advancing bond interface. This *constitutive assumption* is adopted throughout the remainder of the paper.

- **Wafer Release:** Subsequently, the top wafer is released from the retaining chuck of the bonding apparatus. This release allows the remainder of the top wafer to settle onto the bottom wafer under the influence of the propagating interfacial forces and potentially gravitational effects, facilitating the continued expansion of the bonded area.
- **Bond Completion:** The process culminates when the bond interface has propagated across the entire surface of the wafers, resulting in a fully bonded wafer pair.

2.1. The three-dimensional governing equations

Under the assumption of a rigid bottom wafer, the deformation of the top wafer is described by the displacement field

$$\mathbf{u}(\mathbf{X}, t) = (u_1(\mathbf{X}, t), u_2(\mathbf{X}, t), w(\mathbf{X}, t)), \quad \mathbf{X} \in \Omega_{top}, t \in (0, T], \quad (4)$$

where u_1, u_2 denote the in-plane components and w is the out-of-plane (transverse) component. The linearized strain tensor associated with (4) is

$$\boldsymbol{\varepsilon}(\mathbf{u}) = \frac{1}{2}(\nabla \mathbf{u} + \nabla \mathbf{u}^\top). \quad (5)$$

For an isotropic, linearly elastic material, the Cauchy stress tensor is given by the constitutive relation

$$\boldsymbol{\sigma} = \boldsymbol{\sigma}(\boldsymbol{\varepsilon}(\mathbf{u})) = 2G \boldsymbol{\varepsilon}(\mathbf{u}) + \lambda \text{tr}(\boldsymbol{\varepsilon}(\mathbf{u})) \mathbf{I}, \quad (6)$$

where $G = E/[2(1 + \nu)]$ and $\lambda = E\nu/[(1 + \nu)(1 - 2\nu)]$ are the Lamé parameters, E is Young's modulus, and ν is Poisson's ratio.

Under quasi-static conditions, the balance of linear momentum for the top wafer, incorporating all body and surface forces, reads

$$\text{div } \boldsymbol{\sigma}(\mathbf{X}, t) = \mathbf{b}(\mathbf{X}, t) \quad \forall (\mathbf{X}, t) \in \Omega_{top} \times (0, T], \quad (7a)$$

$$\boldsymbol{\sigma} \mathbf{n} = \begin{cases} \mathbf{0}, & \forall (\mathbf{X}, t) \in \partial\Omega_{top}^{lat} \times (0, T], \\ f_S(\mathbf{X}, t) \mathbf{e}_3, & \forall (\mathbf{X}, t) \in \partial\Omega_S \times (0, T], \\ \mathbf{f}^c(\mathbf{X}, t), & \forall (\mathbf{X}, t) \in \partial\Omega_{top}^u \times (0, T], \\ \mathbf{f}_C(\mathbf{X}, t) + \mathbf{f}_B(\mathbf{X}, t) + p(\mathbf{X}, t) \mathbf{n}(\mathbf{x}, t), & \forall (\mathbf{X}, t) \in \partial\Omega_{top}^l \times (0, T], \end{cases} \quad (7b)$$

where:

- $\mathbf{b}(\mathbf{X}, t)$ is the body-force density (e.g., $\mathbf{b} = \{0, 0, b_3\} = -\rho g \mathbf{e}_3$),
- $\mathbf{f}^c(\partial\Omega_{top}^u, t)$ is the contact traction exerted by the chuck on the top surface,
- $\mathbf{f}_B(\mathbf{x}, h)$ is the bonding traction (cf. (3)),

- $\mathbf{f}_c(\mathbf{X}, t)$ is the contact traction preventing inter-penetration of the wafers,
- $p(\mathbf{X}, t)$ is the pressure of the air in the bond gap, which induces the normal load $p(\mathbf{X}, t) \mathbf{n}(\mathbf{X}, t)$ on $\partial\Omega_{top}^l$.

The air pressure p is determined by the three-dimensional Reynolds lubrication equation posed on the gap domain Ω_{gap} with gap height $h(\mathbf{X}, t) = h_0 + w(\mathbf{X}, t)$:

$$12\mu \frac{\partial h}{\partial t} - \nabla \cdot (h^3 \nabla p) = 0, \quad \forall \mathbf{X} \in \Omega_{gap}, t \in (0, T], \quad (8)$$

where μ is the dynamic viscosity of air.

The coupled three-dimensional FSI problem can thus be stated abstractly as:

$$\mathcal{G}_1(\mathbf{u}, p) \equiv \operatorname{div} \boldsymbol{\sigma}(\mathbf{u}) - \mathbf{b} = \mathbf{0}, \quad (9a)$$

$$\mathcal{G}_2(p, \mathbf{u}) \equiv 12\mu \frac{\partial h}{\partial t} - \nabla \cdot (h^3 \nabla p) = 0, \quad (9b)$$

subjected to the traction boundary conditions in Eq. (7b). Here, the coupling is two-way: the displacement \mathbf{u} determines the gap h appearing in \mathcal{G}_2 , and the pressure p enters as a surface traction in \mathcal{G}_1 . This system of governing equations shares structural similarities with models for the nonlinear viscoelasticity of rubber-like solids [17, 18] and the transient response of dielectric elastomers [19]. Such problems have been successfully implemented using the legacy FEniCS computing platform and, more recently, the high-performance FEniCSx framework [12].

2.2. Reduction to the Kirchhoff–Love plate model

Following [13], the three-dimensional problem $\mathcal{G}_1 = \mathbf{0}$, $\mathcal{G}_2 = 0$ and the traction boundary conditions in Eq. (7b) can be reduced to a two-dimensional plate model in the thin-wafer limit $t_w/R \ll 1$. The classical Kirchhoff–Love hypothesis asserts:

- (i) Straight material fibers initially normal to the mid-surface remain straight and normal to the deformed mid-surface (i.e., the transverse shear strains vanish, $\varepsilon_{\alpha 3} = 0$, $\alpha = 1, 2$).
- (ii) The thickness of the plate does not change during deformation (i.e., $\varepsilon_{33} = 0$).

Kinematics. Under these hypotheses, the three-dimensional displacement field (4) reduces to the form

$$u_\alpha(\mathbf{X}, t) = -X_3 \frac{\partial w}{\partial X_\alpha}(\bar{\mathbf{x}}, t), \quad \alpha = 1, 2, \quad u_3(\mathbf{X}, t) = w(\bar{\mathbf{x}}, t), \quad (10)$$

where $\bar{\mathbf{x}} = (X_1, X_2)$ are the in-plane coordinates of the mid-surface ω (cf. (2)) and $w(\bar{\mathbf{x}}, t)$ is the transverse deflection of the mid-surface. In particular, the in-plane displacements are entirely determined by w and its gradient, so that at the mid-surface ($X_3 = 0$)

$$\mathbf{u} \longrightarrow (0, 0, w(\bar{\mathbf{x}}, t)). \quad (11)$$

Substituting (10) into the strain definition (5), the only non-vanishing components of $\boldsymbol{\varepsilon}$ are

$$\varepsilon_{\alpha\beta} = -X_3 \kappa_{\alpha\beta}(\bar{\mathbf{x}}, t), \quad \kappa_{\alpha\beta} = \frac{\partial^2 w}{\partial X_\alpha \partial X_\beta}, \quad \alpha, \beta = 1, 2, \quad (12)$$

where $\boldsymbol{\kappa} = \nabla^2 w$ is the curvature tensor of the mid-surface.

Table 1: Parameters appearing in Section 2.

Symbol	Meaning
Geometric/kinematic parameters	
\mathbf{X}	Reference (material) coordinate in \mathbb{R}^3 ; t denotes time.
$\bar{\mathbf{x}}$	In-plane coordinate on the mid-surface ω .
Ω_{top}	Three-dimensional reference domain of the top wafer.
Ω_{bot}	Three-dimensional reference domain of the bottom wafer.
Ω_{gap}	Thin interstitial air-gap domain between the wafers.
ω	Two-dimensional mid-surface domain of the top wafer (projection of Ω_{top} onto $X_3 = 0$).
$\partial\Omega_{top}^{u,l}$	Top/bottom surfaces of the top wafer; $\partial\Omega_{top}^{lat}$ its lateral surface.
Γ_R	Outer edge of the plate/mid-surface, $\Gamma_R = \{\bar{\mathbf{x}} \in \mathbb{R}^2 : X_1^2 + X_2^2 = R^2\}$.
Γ_{vent}	Vented portion of the boundary where the air gap is open to ambient; here $\Gamma_{vent} = \Gamma_R$.
\mathbf{n}	Outward unit normal.
R	Wafer radius.
t_w	Wafer thickness.
h_0	Initial air-gap height (initial wafer separation).
$h(\mathbf{X}, t)$	Local gap between wafers (here $h = h_0 + w$).
$r_b(t)$	Bond-front radius, i.e. the radial position of the moving bonded/unbonded interface.
R_S	Striker radius.
T	Final time of interest for $t \in (0, T]$.
$\mathbf{u}(\mathbf{X}, t)$	Displacement field; w denotes the transverse displacement component.
$\boldsymbol{\varepsilon}(\mathbf{u})$	Linearized strain tensor.
$\boldsymbol{\sigma}$	Cauchy stress tensor.
Constitutive parameters	
E, ν	Young's modulus and Poisson's ratio.
G, λ	Lamé parameters.
D	Plate flexural rigidity, $D = Et_w^3/[12(1 - \nu^2)]$.
ρ	Mass density.
μ	Dynamic viscosity of air.
Force/loading parameters	
$\mathbf{b}(\mathbf{X}, t)$	Body-force density (e.g., gravity, $\mathbf{b} = -\rho g \mathbf{e}_3$).
g	Gravitational acceleration.
$\mathbf{f}^c(\mathbf{X}, t)$	Chuck contact traction applied on $\partial\Omega_{top}^u$.
$\mathbf{f}_c(\mathbf{X}, t)$	Unilateral contact traction preventing inter-penetration.
$\mathbf{f}_S(\mathbf{X}, t)$	Striker-applied surface traction/force used to initiate contact.
$q_{ext}(\bar{\mathbf{x}}, t)$	Resultant transverse external loading per unit area of the mid-surface.
δ	Critical separation below which bonding forces activate.
$\mathbf{f}_B(\mathbf{X}, h)$	Interfacial bonding traction as a function of gap.
f_{BE}	Constant bonding traction for $h \leq \delta$.
$p(\mathbf{X}, t)$	Pressure of the entrapped air in the gap.
p_{atm}	Ambient (atmospheric) pressure prescribed on Γ_{vent} .

Bending moments. Invoking the plane-stress condition ($\sigma_{33} = 0$) appropriate for thin plates, the in-plane constitutive relation reads

$$\sigma_{\alpha\beta} = \frac{E}{1-\nu^2}[(1-\nu)\varepsilon_{\alpha\beta} + \nu\varepsilon_{\gamma\gamma}\delta_{\alpha\beta}], \quad \alpha, \beta = 1, 2. \quad (13)$$

The bending-moment tensor is obtained by integrating the first moment of the in-plane stress through the thickness:

$$M_{\alpha\beta} = \int_{-t_w/2}^{t_w/2} X_3 \sigma_{\alpha\beta} dX_3 = D[(1-\nu)\kappa_{\alpha\beta} + \nu\kappa_{\gamma\gamma}\delta_{\alpha\beta}], \quad (14)$$

where

$$D = \frac{Et_w^3}{12(1-\nu^2)} \quad (15)$$

is the flexural rigidity of the plate.

Equilibrium. Integration of the three-dimensional balance of linear momentum (7) through the thickness, together with the traction boundary conditions on $\partial\Omega_{top}^u$ and $\partial\Omega_{top}^l$, yields the classical Kirchhoff-Love plate equation (see, e.g., [13] and references therein):

$$D\Delta^2 w - q_{\text{ext}} + p - f_{\text{S}} - f^{\text{C}}(w) - f_{\text{B}}(w) - f_{\text{C}}(w) = 0 \quad \forall \bar{\mathbf{x}} \in \omega, t \in (0, T], \quad (16)$$

where $\Delta^2 \equiv \Delta(\Delta)$ is the biharmonic operator and:

- $q_{\text{ext}}(\bar{\mathbf{x}}, t)$ is the resultant transverse external loading per unit area of the mid-surface, obtained by through-thickness integration of the body force :

$$q_{\text{ext}}(\bar{\mathbf{x}}, t) = \int_{-t_w/2}^{t_w/2} b_3 dX_3, \quad (17)$$

(Here $b_3 := \mathbf{b} \cdot \mathbf{e}_3$ denotes the transverse (X_3) component of the body-force density \mathbf{b} .)

- $p(\bar{\mathbf{x}}, t)$ is the air pressure in the gap,
- $f_{\text{B}}(w)$ is the bonding traction per unit area, and
- $f^{\text{C}}(w)$ and $f_{\text{C}}(w)$ is the unilateral contact forces per unit area as explained in Section 2.5.

Equation (16) is a fourth-order PDE in w that inherits, through the through-thickness integration, all body and surface forces from the original three-dimensional governing equation (7). Note that, in these expressions, the boldface notation for the forces in (7) has been omitted to emphasize that the corresponding terms in the plate equation (16) are scalar transverse components of the forces.

In the same thin-wafer limit, the Reynolds equation (8) reduces to a two-dimensional equation on the mid-surface ω . Introducing the gap

$$h(\bar{\mathbf{x}}, t) = h_0 + w(\bar{\mathbf{x}}, t), \quad (18)$$

with h_0 denoting the initial uniform separation, the two-dimensional pressure equation is

$$12\mu \frac{\partial h}{\partial t} - \nabla \cdot (h^3 \nabla p) = 0 \quad \forall \bar{\mathbf{x}} \in \omega, t \in (0, T]. \quad (19)$$

The reduced two-dimensional coupled FSI problem is therefore stated abstractly as:

$$\tilde{\mathcal{G}}_1(w(\bar{\mathbf{x}}, t), p(\bar{\mathbf{x}}, t)) \equiv D\Delta^2 w - q_{\text{ext}} + p - f_{\text{S}} - f^{\text{C}}(w) - f_{\text{B}}(w) - f_{\text{C}}(w) = 0 \quad \forall \bar{\mathbf{x}} \in \omega, t \in (0, T], \quad (20a)$$

$$\tilde{\mathcal{G}}_2(p(\bar{\mathbf{x}}, t), w(\bar{\mathbf{x}}, t)) \equiv 12\mu \frac{\partial(h_0 + w)}{\partial t} - \nabla \cdot ((h_0 + w)^3 \nabla p) = 0 \quad \forall \bar{\mathbf{x}} \in \omega, t \in (0, T]. \quad (20b)$$

2.3. Boundary and initial conditions

The coupled system (20a)–(20b) is supplemented with the following boundary and initial conditions for uniqueness of solutions.

Mechanical boundary conditions for the plate. On the outer edge $\Gamma_R = \{\bar{\mathbf{x}} \in \mathbb{R}^2 : X_1^2 + X_2^2 = R^2\}$:

$$w(\bar{\mathbf{x}}, t) = w_\Gamma(\bar{\mathbf{x}}, t) \quad \forall \bar{\mathbf{x}} \in \Gamma_R, t \in (0, T], \quad (21a)$$

$$\frac{\partial w}{\partial n}(\bar{\mathbf{x}}, t) = 0 \quad \forall \bar{\mathbf{x}} \in \Gamma_R, t \in (0, T], \quad (21b)$$

where w_Γ is the prescribed displacement at the wafer edge (e.g., from the top chuck constraint or the release of the top wafer from the top chuck) and a zero-slope condition is imposed for a clamped boundary.

On any symmetry boundaries Γ_s (exploited in the quarter-wafer model):

$$\frac{\partial w}{\partial n}(\bar{\mathbf{x}}, t) = 0, \quad M_{nn}(w) = 0 \quad \forall \bar{\mathbf{x}} \in \Gamma_s, t \in (0, T]. \quad (22)$$

Pressure boundary and initial conditions. Let $\Gamma_{\text{vent}} \subseteq \partial\omega$ denote the portion of the mid-surface boundary where the air gap between the wafers is connected to the ambient environment (i.e., the air pressure is prescribed). In the fully vented configuration considered here, we take $\Gamma_{\text{vent}} = \Gamma_R$.

$$p(\bar{\mathbf{x}}, t) = p_{\text{atm}} \quad \forall \bar{\mathbf{x}} \in \Gamma_{\text{vent}}, t \in (0, T], \quad (23a)$$

$$p(\bar{\mathbf{x}}, 0) = p_0(\bar{\mathbf{x}}) \quad \forall \bar{\mathbf{x}} \in \omega, \quad (23b)$$

where p_{atm} is the ambient (atmospheric) pressure and p_0 is the initial pressure distribution (typically $p_0 = p_{\text{atm}}$).

Initial condition for the deflection:

$$w(\bar{\mathbf{x}}, 0) = 0 \quad \forall \bar{\mathbf{x}} \in \omega. \quad (24)$$

2.4. Summary of the coupled problem

For convenience, the complete coupled plate–air FSI problem is collected here. Find the transverse deflection $w(\bar{\mathbf{x}}, t)$ and air pressure $p(\bar{\mathbf{x}}, t)$ on the mid-surface domain ω for $t \in (0, T]$ satisfying:

$$\tilde{\mathcal{G}}_1(w(\bar{\mathbf{x}}, t), p(\bar{\mathbf{x}}, t)) \equiv D \Delta^2 w - q_{\text{ext}} + p - f_s - f^c(w) - f_B(w) - f_C(w) = 0 \quad \forall \bar{\mathbf{x}} \in \omega, t \in (0, T], \quad (25a)$$

$$\tilde{\mathcal{G}}_2(p(\bar{\mathbf{x}}, t), w(\bar{\mathbf{x}}, t)) \equiv 12\mu \frac{\partial h}{\partial t} - \nabla \cdot (h^3 \nabla p) = 0 \quad \forall \bar{\mathbf{x}} \in \omega, t \in (0, T], \quad (25b)$$

$$h(\bar{\mathbf{x}}, t) = h_0 + w(\bar{\mathbf{x}}, t) \quad \forall \bar{\mathbf{x}} \in \omega, t \in (0, T], \quad (25c)$$

with the boundary conditions (21)–(22) for w , the pressure conditions (23), and the initial conditions (24) and (23b). The coupling is two-way: the deflection w modifies the gap h in $\tilde{\mathcal{G}}_2$ and thereby the air-flow resistance, while the air pressure p enters the plate equation $\tilde{\mathcal{G}}_1$ as a distributed transverse load.

2.5. The Contacts

We model contact with the rigid chucks/wafers via (penalty-type) tractions expressed in terms of the transverse deflection w .

Top-chuck contact. Let $k_{\text{top}}^{\text{c}} > 0$ denote a penalty stiffness associated with the rigid top chuck. The corresponding contact traction f^{c} is defined by

$$f^{\text{c}}(\bar{\mathbf{x}}, t) \equiv f^{\text{c}}(w(\bar{\mathbf{x}}, t)) = \begin{cases} k_{\text{top}}^{\text{c}} w(\bar{\mathbf{x}}, t), & \text{if } w(\bar{\mathbf{x}}, t) > 0, \\ 0, & \text{otherwise.} \end{cases} \quad (26)$$

This traction penalizes (and thereby prevents) deformation states with $w(\bar{\mathbf{x}}, t) > 0$ that would violate the geometric constraint imposed by the rigid top chuck.

Bottom-wafer contact. We also introduce a unilateral contact traction f_{c} to prevent interpenetration of the top wafer into the bottom wafer. In general, f_{c} may be defined by an analogous penalty law activated at the closure of the gap. However, as shown in Section 4.2, the Reynold's pressure p is sufficient to enforce the non-penetration constraint in the bonded regions and therefore provides an effective contact penalty. Accordingly, throughout the remainder of the paper we set

$$f_{\text{c}}(w) = 0. \quad (27)$$

3. FEniCSx Implementation

This section details the finite element discretization and solution of the coupled plate–air system (25) using FEniCSx [11]. Exploiting the four-fold symmetry of the circular wafer, we solve on a quarter-domain $\omega_q = \{\bar{\mathbf{x}} \in \omega : X_1 \geq 0, X_2 \geq 0\}$ with appropriate symmetry conditions. The plate equation $\tilde{\mathcal{G}}_1 = 0$ is discretized with a C^0 interior-penalty (C0IP) Kirchhoff–Love formulation [20], and the Reynolds equation $\tilde{\mathcal{G}}_2 = 0$ is discretized with standard continuous Galerkin finite elements. Both fields are solved monolithically.

3.1. Recap of the strong-form equations

For convenience we restate the coupled system (25). Find $w(\bar{\mathbf{x}}, t)$ and $p(\bar{\mathbf{x}}, t)$ satisfying:

Plate equation (from (25a)):

$$D \Delta^2 w(\bar{\mathbf{x}}, t) - q_{\text{ext}}(\bar{\mathbf{x}}, t) + p(\bar{\mathbf{x}}, t) - f_{\text{S}} - f^{\text{c}}(w) - f_{\text{B}}(w) - f_{\text{C}}(w) = 0 \quad \forall \bar{\mathbf{x}} \in \omega_q, t \in (0, T], \quad (28)$$

where D is the flexural rigidity (15) and the bending-moment tensor $M_{\alpha\beta}$ is given by (14). In operator form, $D \Delta^2 w = M_{\alpha\beta, \alpha\beta}$, i.e.,

$$\mathbf{M}(w) = D[(1 - \nu) \boldsymbol{\kappa}(w) + \nu \text{tr}(\boldsymbol{\kappa}(w)) \mathbf{I}], \quad \boldsymbol{\kappa}(w) = \nabla^2 w. \quad (29)$$

Reynolds equation (from (25b)–(25c)):

$$12\mu \frac{\partial h}{\partial t}(\bar{\mathbf{x}}, t) - \nabla \cdot \left(\hat{h}(\bar{\mathbf{x}}, t)^3 \nabla p(\bar{\mathbf{x}}, t) \right) = 0 \quad \forall \bar{\mathbf{x}} \in \omega_q, t \in (0, T], \quad (30)$$

with $\hat{h}(\bar{\mathbf{x}}, t) = h_0 + (1 - \beta)w(\bar{\mathbf{x}}, t)$. Here, $0 < \beta \leq 0.0075$ is a small dimensionless regularization parameter; this choice is necessary to prevent p from becoming unphysical as the gap closes, $w \rightarrow -h_0$.

Boundary conditions. On ω_q the boundary $\partial\omega_q$ is decomposed into:

- *Symmetry edges* $\Gamma_x = \{\bar{\mathbf{x}} \in \partial\omega_q : X_1 = 0\}$ and $\Gamma_y = \{\bar{\mathbf{x}} \in \partial\omega_q : X_2 = 0\}$, where the slope vanishes, $\partial_n w = 0$, and $M_{nn}(w) = 0$ (cf. (22)).
- *Outer arc* $\Gamma_R = \{\bar{\mathbf{x}} \in \partial\omega_q : X_1^2 + X_2^2 = R^2\}$, where displacement Dirichlet conditions $w = w_{\Gamma}$ (cf. (21a)) and the pressure venting condition $p_{\text{air}} = p_{\infty}$ (cf. (23a)) are imposed.

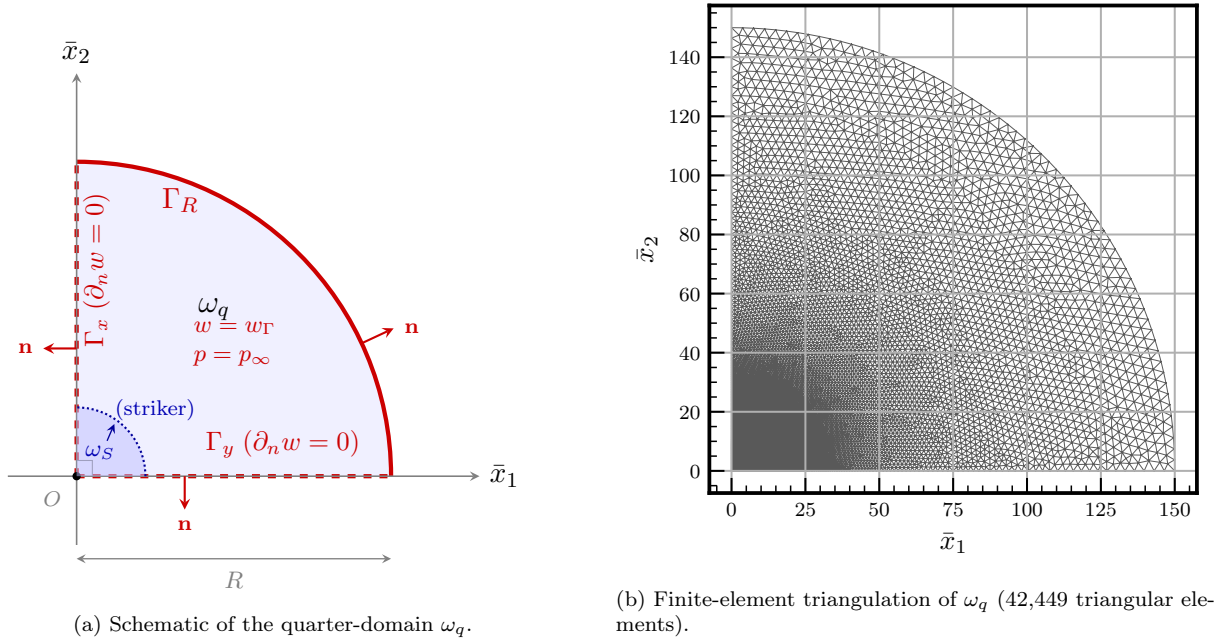


Figure 2: Quarter-domain ω_q exploiting four-fold symmetry of the circular wafer mid-surface ω . (a) Red boundaries: dashed lines denote symmetry edges Γ_x, Γ_y (zero normal slope); solid arc denotes the outer boundary Γ_R (Dirichlet conditions). The striker region ω_S is shown near the origin. (b) The corresponding finite-element mesh (42,449 triangular elements) used in the DOLFINx computation.

3.2. Time discretization

The Reynolds equation (30) is the only equation containing a time derivative. We discretize it with an implicit (backward) Euler scheme. Partitioning $(0, T]$ into time steps $0 = t_0 < t_1 < \dots < t_N = T$ with $\Delta t_n = t_{n+1} - t_n$, and denoting $w^n \approx w(\cdot, t_n)$, $p^{n+1} \approx p_{air}(\cdot, t_{n+1})$, the semi-discrete system at step $n+1$ reads:

$$D \Delta^2 w^{n+1} - q_{ext}^{n+1} + p_{air}^{n+1} - f_S(w^{n+1}) - f^C(w^{n+1}) - f_B(w^{n+1}) - f_C(w^{n+1}) = 0 \quad \forall \bar{\mathbf{x}} \in \omega_q, \quad (31a)$$

$$\frac{12\mu}{\Delta t_n} (w^{n+1} - w^n) - \nabla \cdot (\hat{h}(w^{n+1})^3 \nabla p^{n+1}) = 0 \quad \forall \bar{\mathbf{x}} \in \omega_q. \quad (31b)$$

3.3. Weak formulation

Let $V = H^2(\omega_q)$ and $Q = H^1(\omega_q)$ denote the trial/test spaces for the deflection and pressure fields, respectively, and let $v \in V$, $q \in Q$ be test functions. Multiplying (31a) by v , integrating by parts twice, and multiplying (31b) by q with a single integration by parts, yields the following weak residuals.

Plate residual. Starting from $\int_{\omega_q} M_{\alpha\beta, \alpha\beta} v \, d\omega = 0$, two integrations by parts give

$$\begin{aligned} \mathcal{R}_w(w^{n+1}, p^{n+1}; v) &= \int_{\omega_q} \mathbf{M}(w^{n+1}) : \nabla^2 v \, d\omega + \int_{\omega_q} (p^{n+1} - q_{ext}^{n+1}) v \, d\omega \\ &\quad + \int_{\omega_q} [-f_S(w^{n+1}) - f_B(w^{n+1}) - f^C(w^{n+1}) + f_C(w^{n+1}) w^{n+1}] v \, d\omega \end{aligned} \quad (32)$$

where all boundary terms vanish on Γ_R (essential BC) and on $\Gamma_x \cup \Gamma_y$ (symmetry, $M_{nn} = 0$, $\partial_n w = 0$).

Pressure residual. Multiplying (31b) by q and integrating by parts:

$$\mathcal{R}_p(w^{n+1}, p^{n+1}; q) = \int_{\omega_q} 12\mu (w^{n+1} - w^n) q \, d\omega + \Delta t_n \int_{\omega_q} \hat{h}(w^{n+1})^3 \nabla p^{n+1} \cdot \nabla q \, d\omega, \quad (33)$$

where the boundary flux term vanishes on Γ_R ($p^{n+1} = p_\infty$, Dirichlet) and on the symmetry edges (zero normal flux by symmetry).

3.4. C^0 interior-penalty spatial discretization

Since the plate weak form (32) involves second derivatives of w , it requires H^2 -conforming elements. Instead, we use the C^0 interior-penalty (C0IP) method [20], which employs standard C^0 -continuous Lagrange elements and enforces inter-element C^1 -continuity weakly through penalty terms on interior facets.

Finite element spaces. Let \mathcal{T}_h be a conforming triangulation of ω_q and define the quadratic Lagrange spaces

$$V_h = \{\phi_h \in C^0(\bar{\omega}_q) : \phi_h|_K \in \mathbb{P}_2(K) \ \forall K \in \mathcal{T}_h\}, \quad (34)$$

$$Q_h = \{\psi_h \in C^0(\bar{\omega}_q) : \psi_h|_K \in \mathbb{P}_2(K) \ \forall K \in \mathcal{T}_h\}, \quad (35)$$

and the mixed space $W_h = V_h \times Q_h$.

Interior-penalty terms. Let \mathcal{F}_h^i denote the set of interior facets of \mathcal{T}_h , and for any facet $e \in \mathcal{F}_h^i$ let \mathbf{n}_e be a fixed unit normal, h_e the facet diameter, and define the average $\{\{\cdot\}\}$ and jump $[\cdot]$ operators. The normal bending moment and normal slope on a facet are

$$M_{nn}(w_h) = \mathbf{n}_e \cdot \mathbf{M}(w_h) \mathbf{n}_e, \quad [\partial_n w_h] = [\nabla w_h \cdot \mathbf{n}_e]. \quad (36)$$

The C0IP bending residual, replacing the continuous form (32), reads

$$\begin{aligned} \mathcal{R}_w^h(w_h^{n+1}, p_h^{n+1}; v_h) &= \int_{\omega_q} \mathbf{M}(w_h^{n+1}) : \nabla^2 v_h \, d\omega \\ &\quad - \int_{\mathcal{F}_h^i} \{\{M_{nn}(w_h^{n+1})\}\} [\partial_n v_h] \, d\Gamma - \int_{\mathcal{F}_h^i} \{\{M_{nn}(v_h)\}\} [\partial_n w_h^{n+1}] \, d\Gamma \\ &\quad + \int_{\mathcal{F}_h^i} \frac{\alpha_{\text{ip}} D}{h_e} [\partial_n w_h^{n+1}] [\partial_n v_h] \, d\Gamma + \int_{\omega_q} (p_h^{n+1} - q_{\text{ext}}^{n+1}) v_h \, d\omega \\ &\quad + \int_{\omega_q} [-f_S(w_h^{n+1}) - f_B(w_h^{n+1}) - f^C(w_h^{n+1}) + f_C(w_h^{n+1}) w_h^{n+1}] v_h \, d\omega, \end{aligned} \quad (37)$$

where $\alpha_{\text{ip}} > 0$ is the interior-penalty parameter.

On the symmetry boundaries $\Gamma_s \in \{\Gamma_x, \Gamma_y\}$, the condition $\partial_n w = 0$ (cf. (22)) is enforced weakly via Nitsche-type terms consistent with the C0IP formulation:

$$\mathcal{R}_{\text{sym}}^h(w_h^{n+1}; v_h) = \sum_{\Gamma_s \in \{\Gamma_x, \Gamma_y\}} \left[- \int_{\Gamma_s} M_{nn}(w_h^{n+1}) \partial_n v_h \, d\Gamma - \int_{\Gamma_s} M_{nn}(v_h) \partial_n w_h^{n+1} \, d\Gamma + \int_{\Gamma_s} \frac{\alpha_{\text{ip}} D}{h_e} \partial_n w_h^{n+1} \partial_n v_h \, d\Gamma \right]. \quad (38)$$

The discrete pressure residual is identical to the continuous form (33) restricted to Q_h :

$$\mathcal{R}_p^h(w_h^{n+1}, p_h^{n+1}; q_h) = \int_{\omega_q} 12\mu (w_h^{n+1} - w_h^n) q_h \, d\omega + \Delta t_n \int_{\omega_q} \hat{g}(w_h^{n+1})^3 \nabla p_h^{n+1} \cdot \nabla q_h \, d\omega. \quad (39)$$

3.5. Monolithic nonlinear system and Newton solver

The fully discrete monolithic residual is assembled as

$$\mathcal{R}^h(w_h^{n+1}, p_h^{n+1}; v_h, q_h) = \mathcal{R}_w^h(w_h^{n+1}, p_h^{n+1}; v_h) + \mathcal{R}_{\text{sym}}^h(w_h^{n+1}; v_h) + \mathcal{R}_p^h(w_h^{n+1}, p_h^{n+1}; q_h). \quad (40)$$

At each time step t_{n+1} , we seek $(w_h^{n+1}, p_h^{n+1}) \in W_h$ such that

$$\mathcal{R}^h(w_h^{n+1}, p_h^{n+1}; v_h, q_h) = 0 \quad \forall (v_h, q_h) \in W_h^0, \quad (41)$$

where $W_h^0 \subset W_h$ incorporates homogeneous essential boundary conditions ($v_h = 0$ on Γ_R , $q_h = 0$ on Γ_{vent}). The essential (Dirichlet) conditions enforced are:

- $p_h^{n+1} = 0$ on the vented outer boundary Γ_R (gauge pressure),
- $w_h^{n+1} = w_{\text{edge}}(t_{n+1})$ on Γ_R ,
- $w_h^{n+1} = w_{\text{center}}(t_{n+1})$ at the striker/pin region.

Due to the nonlinear loading terms $f_B(w)$, $f_c(w)$, $f_{\text{tc}}(w)$ and the cubic gap dependence $\hat{g}(w)^3$ in the Reynolds equation, the discrete problem (41) is nonlinear and is solved by Newton's method. Denoting the algebraic unknown vector $\mathbf{U} = (\omega_h, \mathbf{p}_h)^\top$ and the algebraic residual vector $\mathbf{R}(\mathbf{U})$, the Newton iteration reads

$$\mathbf{J}(\mathbf{U}^{(k)}) \Delta \mathbf{U}^{(k)} = -\mathbf{R}(\mathbf{U}^{(k)}), \quad \mathbf{U}^{(k+1)} = \mathbf{U}^{(k)} + \Delta \mathbf{U}^{(k)}, \quad (42)$$

where the Jacobian $\mathbf{J} = \partial \mathbf{R} / \partial \mathbf{U}$ is computed automatically via UFL's [16] symbolic differentiation capabilities in FEniCSx.

The complete solution procedure is summarized in Algorithm 1.

4. Results

This section presents the numerical results for the wafer-bonding model; the solution workflow is outlined in Algorithm 1. We first validate the implementation against experimental displacement measurements and illustrate the resulting quarter-symmetric displacement field (Figure 4). We then verify the force balance at the bond front by comparing the Reynolds air pressure with the computed contact reaction (Section 4.2). Next, we assess how the initial bond gap affects air-pressure build-up and the bond-front propagation speed (Section 4.3), and we conduct a parametric study on the role of air viscosity. Finally, we examine how the interfacial energy influences the bonding speed.

4.1. Validation

To validate the implementation, we performed three simulations corresponding to the bond gaps (a) $h_0 = 30 \mu\text{m}$, (b) $h_0 = 70 \mu\text{m}$, and (c) $h_0 = 100 \mu\text{m}$. In each case, Dirichlet boundary condition $w = w_\Gamma$ was prescribed using the displacement history reported in Figure 3 of [6]. The resulting displacement time history at the mid-region of the top wafer was then compared with the experimental probe measurements. Figure 3 shows that the model reproduces the measured response with good qualitative agreement and reasonable quantitative accuracy. Small discrepancies are expected because several inputs required for an exact match are not fully specified in [6] (e.g., interfacial energy and the precise probe location); these were therefore inferred through a calibration procedure in this work. The effect of air pressure is evident in both the experiments and the simulations. In contrast to what is expected for bonding in the absence of air (pure-plate-bending), in the presence of air, bonding proceeds fastest for the largest initial bond gap and slowest for the smallest bond gap. This trend is also evident in Section 4.3.

Snapshots of the simulated out-of-plane displacement field are shown as 2D contour plots at selected time instants in Figure 4.

Algorithm 1 Monolithic coupled wafer-wafer bonding simulation in FEniCSx

```
1: // -- Mesh, FE Spaces & Measures --
2: Load Gmsh model via gmsh.model_to_mesh → mesh  $\mathcal{T}_h$ ; build connectivity
3:  $h_{ip} \leftarrow \sqrt{|\omega_q|/N_{\text{cells}}}$  IP penalty scale
4:  $W_h \leftarrow \text{functionspace}(\text{msh}, \text{mixed\_element}([P2, P2]))$ 
5:  $(w_h, p_h), (v_h, q_h), (w_h^n, p_h^n) \leftarrow \text{split}$  of trial, test, prev. step Functions
6:  $\mathbf{dx}, \mathbf{dS} \leftarrow \text{cell/interior-facet}$  measures;  $\mathbf{ds\_sym} \leftarrow \text{tagged}$  symmetry facets via meshtags

7: // -- UFL Variational Forms --
8: ▷ Plate residual  $\mathcal{R}_w^h$  (37):  $F1 \leftarrow \text{inner}(\mathbf{M}, \text{hess}) * \mathbf{dx} - \text{avg}(\mathbf{M\_nn}) * \text{jump} * \mathbf{dS} + \text{penalty} + \text{loads}$ 
9: ▷ Nitsche symmetry  $\mathcal{R}_{\text{sym}}^h$  (38):  $F1 += \sum_{\Gamma_s} [-\mathbf{M\_nn} * \text{dn\_v} + \alpha D / h * \text{dn\_w} * \text{dn\_v}] * \mathbf{ds\_sym}$ 
10: ▷ Pressure residual  $\mathcal{R}_p^h$  (39):  $F2 \leftarrow 12\mu(w - \text{wn}) * \mathbf{q} * \mathbf{dx} + \Delta t * \hat{g}^3 * \text{dot}(\text{grad}(p), \text{grad}(q)) * \mathbf{dx}$ 
11:  $\text{residual} \leftarrow F1 + F2$ ;  $\text{jacobian} \leftarrow \text{derivative}(\text{residual}, w\_p, \text{TrialFunction})$  [16]

12: // -- Boundary Conditions & Solver --
13:  $\text{bcs} \leftarrow [\text{dirichletbc}(p=0, \Gamma_R), \text{dirichletbc}(w=w_{\text{edge}}, \Gamma_R), \text{dirichletbc}(w=w_{\text{ctr}}, \omega_S)]$ 
14:  $\text{problem} \leftarrow \text{NonlinearProblem}(\text{residual}, w\_p, \text{bcs}, \mathbf{J}=\text{jacobian})$ ; PETSc LU/MUMPS
15: Open VTXWriter for  $w, p$  output (BP4)

16: // -- Time-Stepping Loop --
17: for  $n = 0, 1, \dots, N-1$  do
18:    $t_{n+1} \leftarrow t_n + \Delta t_n$ ; update dt.value, disp\_edge.value, disp\_center.value from CSV
19:   Solve:  $\text{problem.solve}()$  assembles  $\mathbf{R}, \mathbf{J}$ ; Newton iteration (42)
20:    $w\_p\_n.x.array[:] = w\_p.x.array[:]$ ;  $w\_sol.interpolate(w\_sub)$ 
21:    $w\_vtx.write(t_{n+1})$ ;  $p\_vtx.write(t_{n+1})$  write output
22: end for

23:  $w\_vtx.close()$ ;  $p\_vtx.close()$ ; save radial profiles via np.save
24: return  $(w_h^N, p_h^N)$ 
```

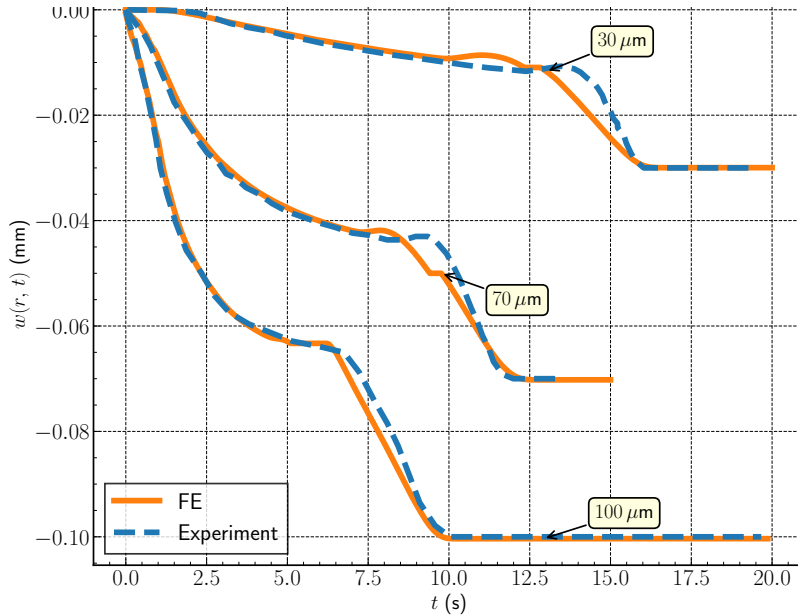


Figure 3: Top wafer displacement $w(r, t)$ versus time at a fixed radial location $r = \text{mid-region}$ for $h_0 = 30, 70,$ and $100 \mu\text{m}$. Solid lines (orange) show the finite-element solution; dashed lines (blue) show the experimental measurement.

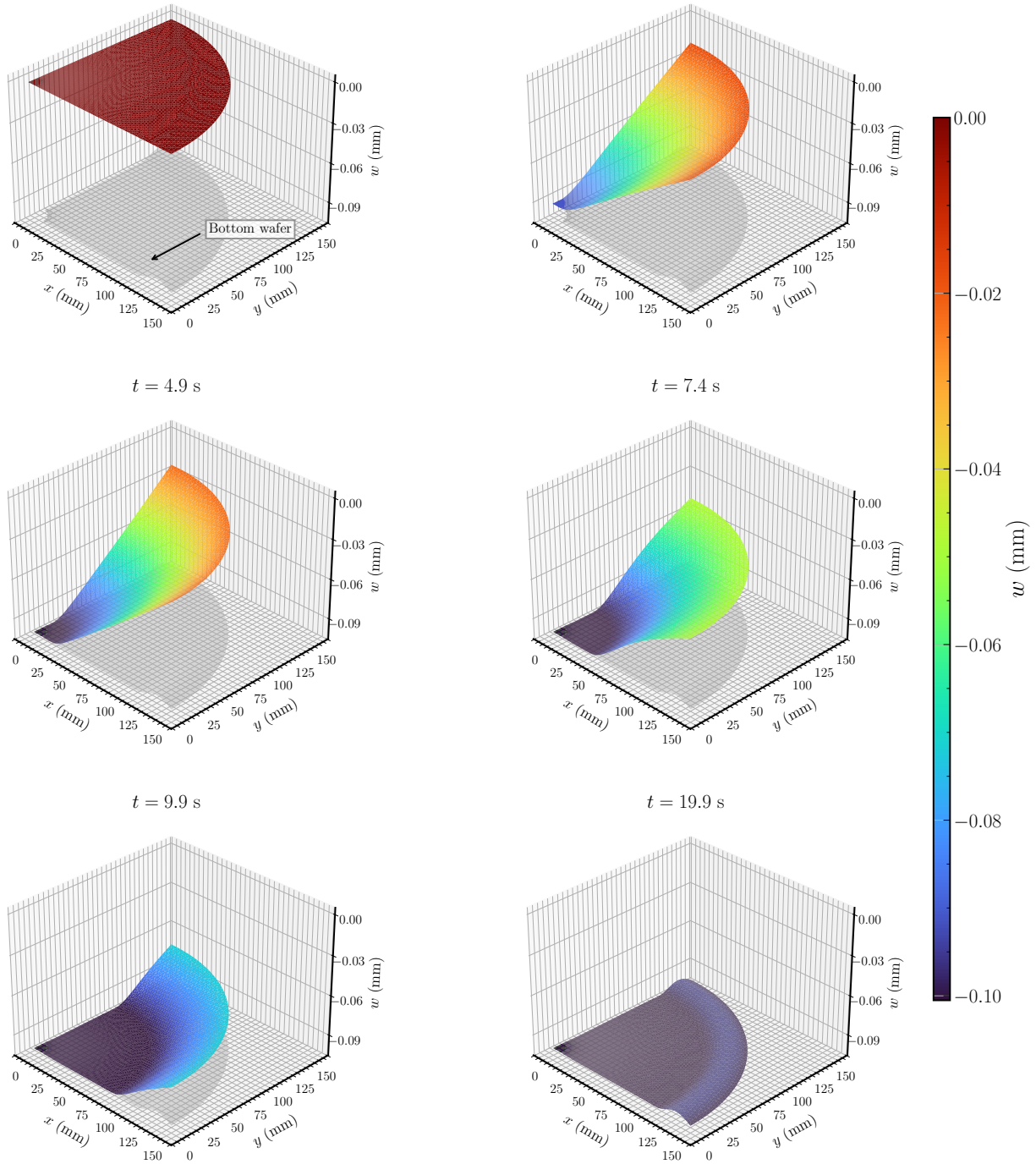


Figure 4: Snapshots of the displacement field w at nine time instances during bonding ($h = 70 \mu\text{m}$ gap). The out-of-plane displacement is warped by a factor of 500 to enhance the visualisation. The bottom wafer shape is represented by the gray shape, and the colormap indicates the out-of-plane displacement of the top wafer.

4.2. Reynold's pressure acting as a contact force

As discussed in Section 2.5, we set the bottom-wafer contact tractions to zero, $f_c(w) = 0$, because the air-film pressure obtained from the Reynolds solution, p , is sufficient to enforce non-penetration contact. This can be seen from Eq. (30): the Reynolds equation is solved over the full computational domain ω , including regions that are already bonded. In the bonded region the Reynolds pressure acts as a reaction pressure, i.e., an effective contact traction that prevents interpenetration of the wafers. Figure 5 confirms this interpretation by showing that the Reynolds pressure behind the bond front balances the applied striker pressure. So, at the bond front,

$$p(\bar{\mathbf{x}}, t) = \bar{p}(\bar{\mathbf{x}}, t) + p_{\text{air}}(\bar{\mathbf{x}}, t), \quad (43)$$

where, p_{air} is the actual pressure due to the air between the two wafers in the unbonded region.

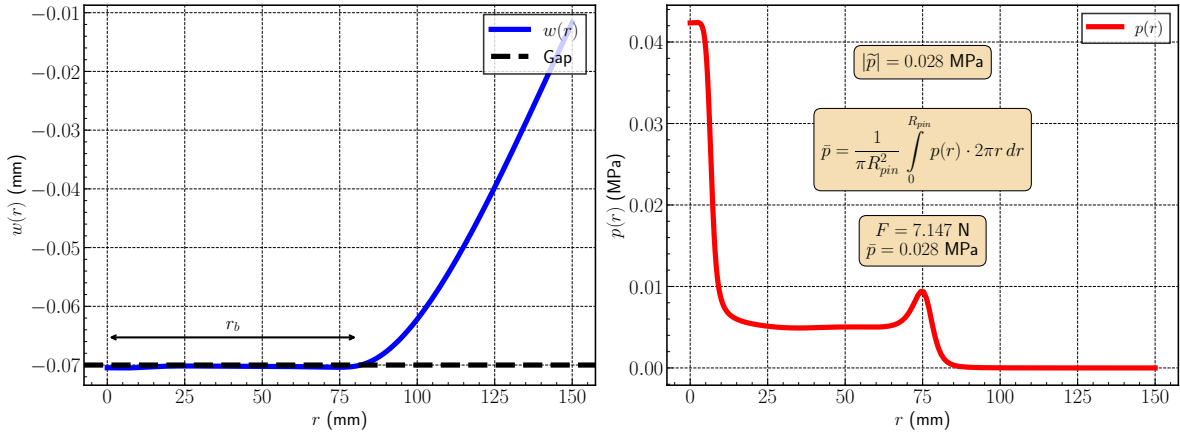


Figure 5: Displacement $w(r)$ (left) and pressure $p(r)$ (right) at the final time step ($t = 50$ s) for a $70\ \mu\text{m}$ gap. The average pressure \bar{p} computed by integrating the Reynolds pressure over the bonded area ($r \leq R_{\text{pin}}$) equals the applied pressure $|\bar{p}|$, verifying force equilibrium across the bonding front. This confirms that the Reynolds pressure field correctly captures the contact mechanics at the bond front.

4.3. Effect of bond gap on bond speed

In this section, we examine the bonding speed for the three bond gaps considered in the validation exercise in Section 4.1. As shown in Fig. 6, the response is nonlinear and non-monotonic. Unlike bonding in the absence of air (pure plate bending), bonding completes earliest for the largest bond gap than for the smallest gap; see Fig. 6(a). This ordering is driven by the air-film pressure p_{air} in the unbonded region: smaller gaps generate higher p_{air} , which increases the resistance to bond-front advance. The bond-front speed is also nonlinear because it depends on the extent of the unbonded region at the current bond-front location, as illustrated in Fig. 6(c). This non-monotonic behavior is expected, since the bond-front speed and the evolution of air pressure are governed by Reynolds' equation. Additional validation plots for the spatio-temporal displacement fields and radial air-pressure snapshots are provided in Appendix A; see Figs. 9 and 10.

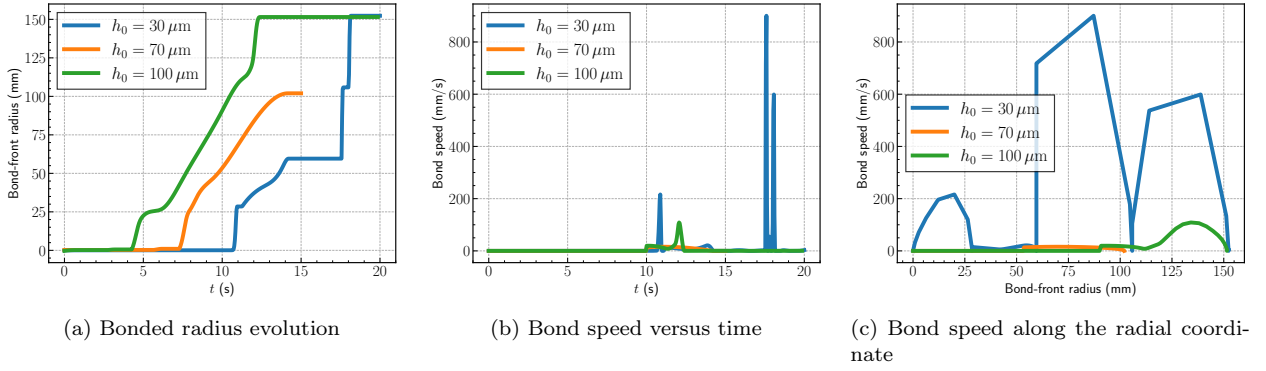


Figure 6: Bond speed diagnostics for three bond gaps: (a) bonded radius versus time, (b) bond speed versus time, and (c) bond speed versus radial position for $h = 30, 70,$ and $100 \mu\text{m}$.

4.4. Effect of Air Viscosity on air pressure and Bond Speed

Varying the air viscosity modifies the Reynolds pressure field and, consequently, the bond-front propagation rate. Figure 7 summarises the post-processed diagnostics used to quantify this effect: bond speed versus time, the spatial variation of bond speed, and the temporal evolution of the bonded radius. For the same time instant, lower viscosity yields a faster bond front and a larger bonded area.

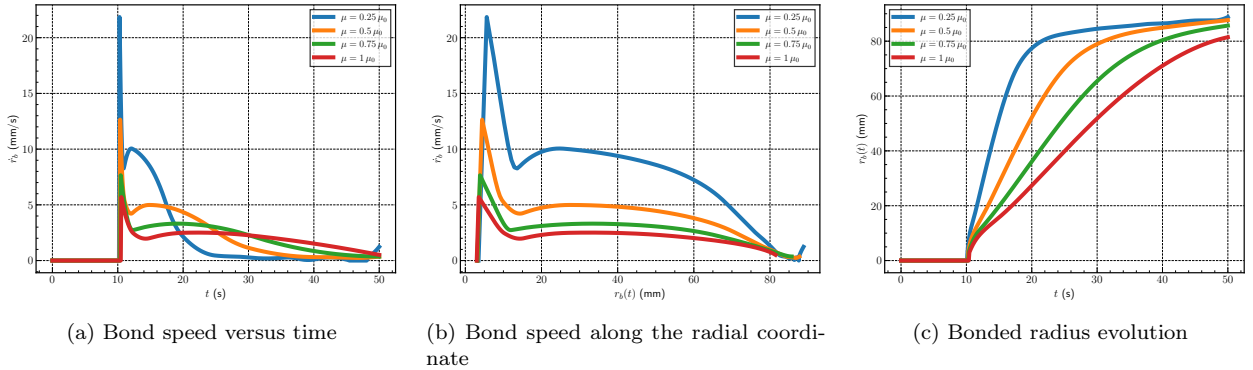


Figure 7: Effect of air viscosity on: (a) bond speed over time, (b) bond speed versus radius, and (c) temporal growth of the bonded radius.

4.5. Effect of Interfacial Energy on bond speed

Varying the interfacial energy γ changes the thermodynamic driving force for bonding, which in turn affects the bond speed. Figure 8 presents the diagnostics that capture this sensitivity: the bond speed as a function of time, the spatial distribution of the bond speed, and the temporal evolution of the bonded radius.

5. Conclusion and Future Work

5.1. Conclusions

This work developed a mathematically consistent reduced-order model for wafer-to-wafer bonding by coupling a Kirchhoff–Love plate description of wafer bending to a Reynolds lubrication model for the entrapped air film. Starting from three-dimensional linear elasticity, the plate equation was obtained in the thin-wafer limit and combined with a pressure evolution law in which the wafer

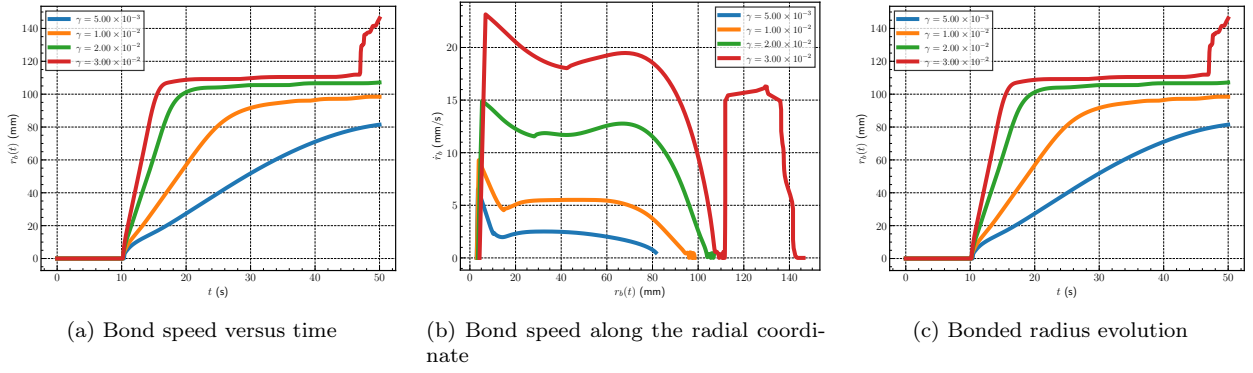


Figure 8: Interfacial energy sensitivity diagnostics: (a) bond speed over time, (b) bond speed versus radius, and (c) temporal growth of the bonded radius. Higher interfacial energy accelerates the bond front and increases the bonded area for equal time stamps.

deflection directly modulates the local gap height and flow resistance. The resulting nonlinear, strongly coupled system was discretized in a monolithic manner and implemented in the FEniCSx framework using a C^0 interior-penalty formulation for the fourth-order plate operator together with standard continuous Galerkin elements for the pressure field. The numerical studies demonstrated consistent force balance in the contact region and produced bonding-front dynamics in agreement with experimentally measured probe-displacement histories, thereby providing a predictive and computationally efficient tool for assessing process sensitivities.

A key advantage of the present formulation is that the coupling structure is explicit: the air pressure enters the plate equation as a distributed transverse load, while the plate deflection enters the Reynolds equation through the evolving gap $h = h_0 + w$. This structure enables systematic extensions of the physics without altering the overall solution strategy.

5.2. Extension to anisotropic flexural response

In the current isotropic plate model, the bending stiffness enters through the scalar flexural rigidity $D = Et_w^3/[12(1 - \nu^2)]$. For crystalline wafers and layered stacks, however, the effective bending response can be direction-dependent. Within the same Kirchhoff–Love framework, anisotropy can be incorporated by replacing the scalar stiffness with a bending-stiffness tensor. In practice, one introduces the bending moment–curvature relation

$$\mathbf{M} = \mathbb{D} \boldsymbol{\kappa}, \quad (44)$$

where \mathbf{M} and $\boldsymbol{\kappa} = \nabla^2 w$ are the bending-moment and curvature tensors, respectively, and \mathbb{D} is a symmetric fourth-order bending stiffness (often expressed, under plane-stress reduction, as a 3×3 matrix in Voigt notation). The plate equilibrium then becomes

$$\nabla \cdot \nabla : (\mathbb{D} \boldsymbol{\kappa}) - q_{ext} + p_{air} - f_B(w) - f_c(w) = 0, \quad (45)$$

which reduces to $D \Delta^2 w$ when \mathbb{D} corresponds to isotropic bending. Because the Reynolds equation and the coupling through h remain unchanged, the anisotropic extension primarily modifies the plate operator and the constitutive evaluation of bending moments, and can be integrated into the present monolithic Newton framework with minimal changes.

5.3. Future work

Several extensions are planned. First, we will incorporate anisotropic and heterogeneous bending stiffness to represent crystallographic effects, device layers, and patterned stacks, enabling more

accurate prediction of bonding kinetics for modern wafer architectures. Second, we will extend the reduced two-dimensional plate–Reynolds formulation to a geometrically richer shell model. A shell description will allow simultaneous prediction of (i) bond-front propagation and pressure evolution in the interfacial air film and (ii) in-plane deformations, including wafer stretch, shear, and in-plane distortion. This, in turn, will enable prediction of post-bond wafer shapes and residual distortions (e.g., global bow/warp and in-plane misfit patterns) that are critical for overlay, alignment, and downstream process yield. Finally, we will investigate model calibration and uncertainty quantification using additional metrology signals (e.g., full-field displacement/shape measurements) to improve robustness across tool configurations and process conditions.

Appendix A Additional validation results for Section 4.1

This appendix collects additional plots supporting the validation study in Section 4.1.

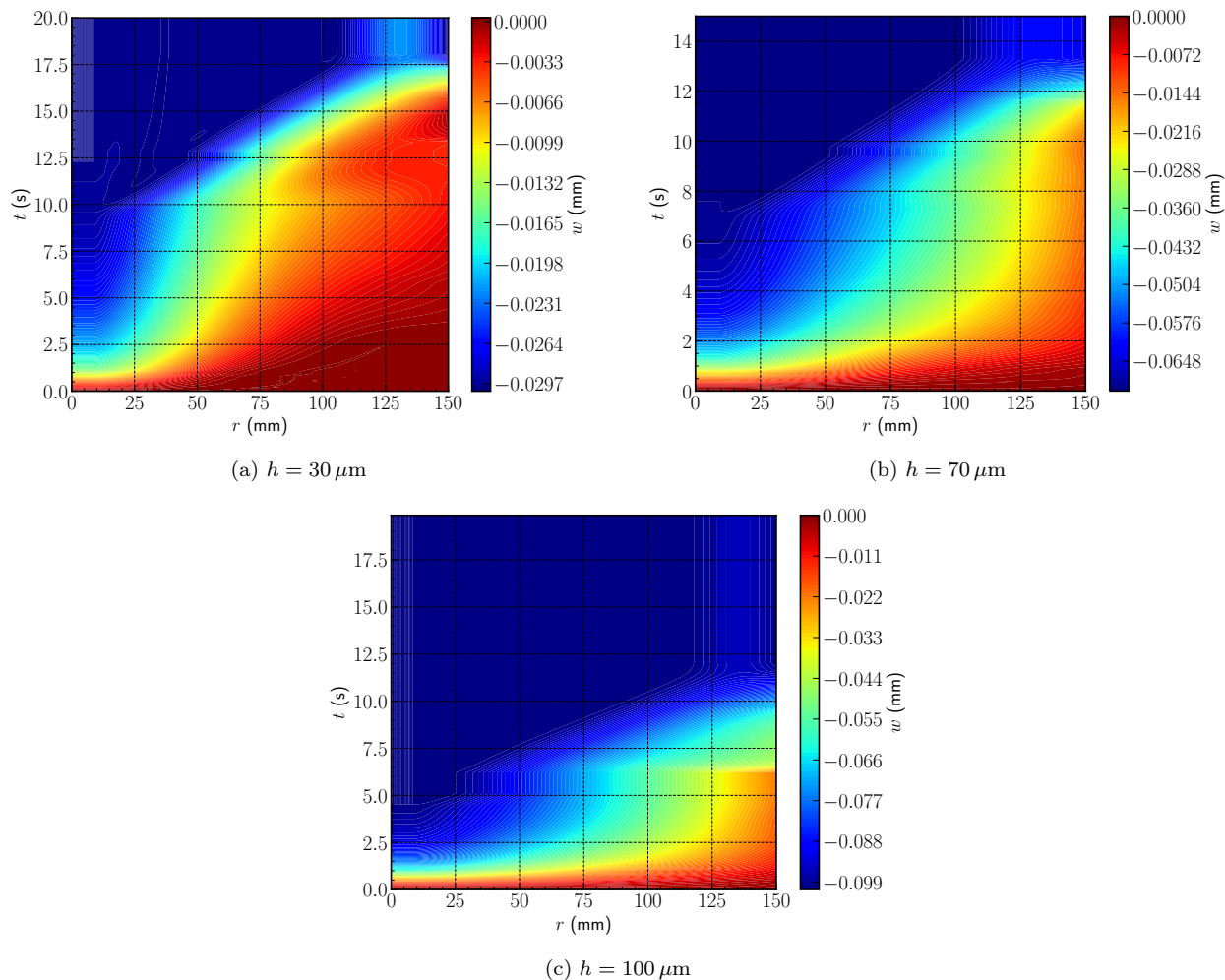


Figure 9: Spatio-temporal evolution of the radial displacement field $w(r, t)$ for three bond gaps.

References

- [1] Shuyu Bao, Yue Wang, Khaw Lina, Li Zhang, Bing Wang, Wardhana Aji Sasangka, Kenneth Eng Kian Lee, Soo Jin Chua, Jurgen Michel, Eugene Fitzgerald, Chuan Seng Tan, and Kwang Hong Lee. A review of silicon-based wafer bonding processes, an approach to realize

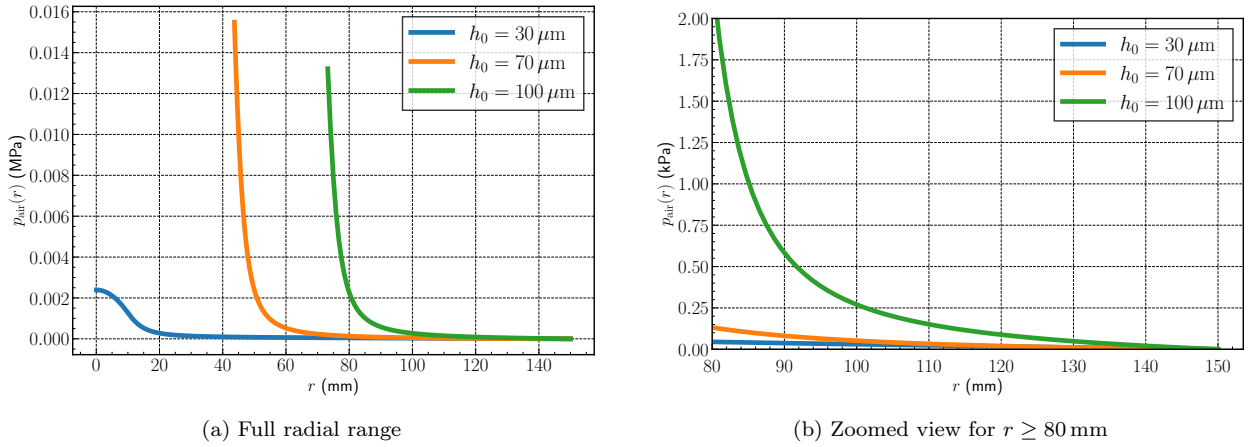


Figure 10: Radial air-pressure profiles $p_{\text{air}}(r)$ in the unbonded region, $r > r_b(t)$, for $h_0 = 30, 70,$ and $100 \mu\text{m}$, evaluated at the common time $t = 9$ s: (a) full radial range and (b) zoomed view for the outer region near the bond front.

the monolithic integration of Si-CMOS and III-V-on-Si wafers. *Journal of Semiconductors*, 42(2):023106, 2021. doi: 10.1088/1674-4926/42/2/023106.

- [2] H. Moriceau, F. Rieutord, F. Fournel, Y. Le Tiec, L. Di Cioccio, C. Morales, A. M. Charvet, and C. Deguet. Physics of direct bonding: Applications to 3D heterogeneous or homogeneous integration. *Microelectronics Reliability*, 50(8):1154–1162, 2010. doi: 10.1016/j.microrel.2010.01.011.
- [3] F. Rieutord, B. Bataillou, and H. Moriceau. Dynamics of a bonding front. *Physical Review Letters*, 94:236101, 2005. doi: 10.1103/PhysRevLett.94.236101.
- [4] E. Navarro et al. Direct silicon bonding dynamics: a coupled fluid/structure analysis. *Applied Physics Letters*, 103:034104, 2013. doi: 10.1063/1.4813843.
- [5] D. Radisson, F. Fournel, and E. Charlaix. Modelling of the direct bonding wave. *Microsystem Technologies*, 21:969–971, 2015. doi: 10.1007/s00542-014-2101-y.
- [6] Nathan Ip, Nima Nejadsadeghi, Carlos Fonseca, Norifumi Kohama, and Kimio Motoda. Multiphysics simulation of wafer-to-wafer bonding dynamics. In *2022 IEEE 72nd Electronic Components and Technology Conference (ECTC)*, pages 502–506. IEEE, 2022.
- [7] Kyeongbin Lim et al. Design and simulation of symmetric wafer-to-wafer bonding compensating a gravity effect. In *2020 IEEE 70th Electronic Components and Technology Conference (ECTC)*, pages 1480–1485. IEEE, 2020. doi: 10.1109/ECTC32862.2020.00233.
- [8] Feixiang Tang, Siyu He, Yuhan Li, Wenjin Liu, Fang Dong, and Sheng Liu. Numerical and mechanical analysis of direct wafer bonding considering non-uniform impurity particle distributions. *Microsystems & Nanoengineering*, 11:151, 2025. doi: 10.1038/s41378-025-00994-4.
- [9] Seyed Amir Fouad Farshchi Yazdi, Matteo Garavaglia, Aldo Ghisi, and Alberto Corigliano. An experimental and numerical study on glass frit wafer-to-wafer bonding. *Micromachines*, 14(1):165, 2023.
- [10] Yan Wen Tsau, Joke De Messemaeker, Abdellah Salahouelhadj, Mario Gonzalez, Liesbeth Witters, Boyao Zhang, Marc Seefeldt, Eric Beyne, and Ingrid De Wolf. Simulation of Cu pad

- expansion in wafer-to-wafer Cu/SiCN hybrid bonding. *Microelectronics Reliability*, 138:114716, 2022.
- [11] Igor A Baratta, Joseph P Dean, Jørgen S Dokken, Michal Habera, Jack Hale, Chris N Richardson, Marie E Rognes, Matthew W Scroggs, Nathan Sime, and Garth N Wells. DOLFINx: the next generation FEniCS problem solving environment. *Zenodo*, 2023. doi: 10.5281/zenodo.10447666. URL <https://doi.org/10.5281/zenodo.10447666>. Preprint.
- [12] Kamalendu Ghosh and Bhavesh Shrimali. A hybrid finite element implementation of two-potential constitutive model of dielectric elastomers. *Finite Elements in Analysis and Design*, 247:104348, 2025.
- [13] Bhavesh Shrimali, Matteo Pezulla, Samuel Poincloux, Pedro M Reis, and Oscar Lopez-Pamies. The remarkable bending properties of perforated plates. *Journal of the Mechanics and Physics of Solids*, 154:104514, 2021.
- [14] Matthew W Scroggs, Jørgen S Dokken, Chris N Richardson, and Garth N Wells. Construction of arbitrary order finite element degree-of-freedom maps on polygonal and polyhedral cell meshes. *ACM Transactions on Mathematical Software*, 48(2):1–23, 2022.
- [15] Matthew W Scroggs, Igor A Baratta, Chris N Richardson, and Garth N Wells. Basix: a runtime finite element basis evaluation library. *Journal of Open Source Software*, 7(73):3982, 2022.
- [16] Martin S Alnæs, Anders Logg, Kristian B Ølgaard, Marie E Rognes, and Garth N Wells. Unified form language: A domain-specific language for weak formulations of partial differential equations. *ACM Transactions on Mathematical Software*, 40(2):1–37, 2014.
- [17] Kamalendu Ghosh, Bhavesh Shrimali, Aditya Kumar, and Oscar Lopez-Pamies. The nonlinear viscoelastic response of suspensions of rigid inclusions in rubber: I—Gaussian rubber with constant viscosity. *Journal of the Mechanics and Physics of Solids*, 154:104544, 2021.
- [18] Bhavesh Shrimali, Kamalendu Ghosh, and Oscar Lopez-Pamies. The nonlinear viscoelastic response of suspensions of vacuuous bubbles in rubber: I—Gaussian rubber with constant viscosity. *Journal of Elasticity*, 153(4):479–508, 2023.
- [19] Kamalendu Ghosh and Oscar Lopez-Pamies. On the two-potential constitutive modeling of dielectric elastomers. *Meccanica*, 56(6):1505–1521, 2021.
- [20] Tom Gustafsson, Rolf Stenberg, and Juha Videman. On Nitsche’s method for elastic contact problems. *SIAM Journal on Scientific Computing*, 42(2):B425–B446, 2020.